Nanoscale

Accepted Manuscript

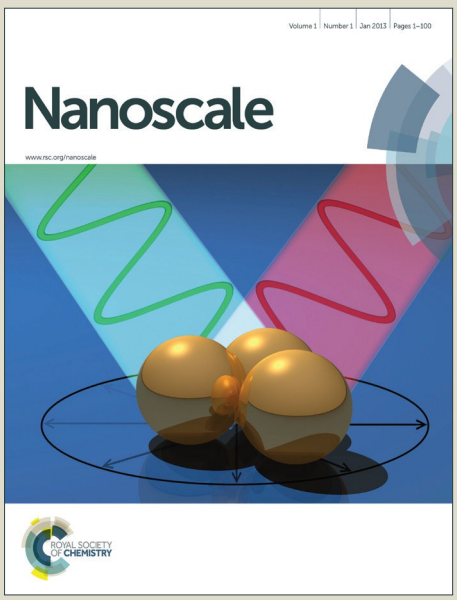

ROYAL SOCIETY OF CHEMISTRY

www.rsc.org/nanoscale

Layered nano-gratings by electron beam writing to form 3-level diffractive optical elements for 3D phase-offset holographic lithography

Liang (Leon) Yuan* and Peter R. Herman
The Edward S. Rogers Sr. Department of Electrical and Computer Engineering and Institute for Optical Sciences, University of Toronto, 10 King's College Road, Toronto, Ontario, M5S 3G4, Canada
**Email: leon.yuan@mail.utoronto.ca*

Abstract: Multilevel nanophotonic structure is a major goal in providing advanced optical functionalities such as found in photonics crystals and metamaterials. A three-level nano-grating phase mask has been fabricated in electron-beam resist (ma-N) to meet with the requirement for holographic generation of diamond-like 3D nanostructure in photoresist in a single exposure step. A 2D mask with 600 nm periodicity is presented for generating first order diffracted beams with preferred $\pi/2$ phase shift on the X- and Y-axes and with sufficient 1^{st} order diffraction efficiency of 3.5% at 800 nm wavelength for creating 3D periodic nanostructure in SU-8 photoresist. The resulting 3D structure is anticipated to provide an 8% complete PBG upon silicon inversion. A thin SiO_2 layer was used to isolate the grating layers and multiple spin-coating steps served to planarize the final resist layer. A reversible soft coating (aquaSAVE) was introduced to enable SEM inspection and verification of each insulating grating layer. This e-beam lithographic method is extensible to assembling multiple layers of nanophotonic structure.

1. Introduction

Phase mask lithography has become a widely used method in fabricating a variety of three-dimensional (3D) periodic nanostructures [1-8] owing to the inherent stability of phase-locked interfering beams and the rapid fabrication time. Typical binary masks of 2D square symmetry are limited in producing body centered tetragonal (BCT) structures in photosensitive materials with potential only for generating directional stopbands or partial photonic band gaps (PBGs) [1, 2]. Hence, multi-level phase masks with phase-shift control are more desirable in offering favorable symmetry that benefits the formation of complete PBGs [3, 4] when using materials with sufficiently high refractive index. However, the formation of PBGs in the visible or telecommunication spectrum imposes significant demands on the phase mask design [5, 6], requiring precise multi-layered structuring of optical elements with 100-nm resolution.

A variety of lithographic and processing techniques have been demonstrated that enable high resolution nanopatterning of single-layered optical materials, which in turn can be assembled into 3D nanostructures with multiple processing steps. Electron beam lithography together with layer-by-layer assembly enabled the formation of a 3D photonic crystal in III-V semiconductors to offer a complete PBG [9]. Focused ion beam milling has further provided high resolution subtractive processing to form 3D metamaterial with alternating dielectric and metallic layers [10]. However, such methods have not been widely applied in forming phase masks for interference holography of 3D photonic crystal templates [11]. Gray-scale lithographic processing provides variable level diffractive optics, for example in polymer [12], photosensitive hybrid glasses [13] or diamond [14], but is challenging to scale down to the hundreds of nm resolution. Alternatively, multi-level phase masks with approximately 1-µm grating periods have been laser-structured in photoresist and glass but lack precision in phase registration of the gratings [6, 15, 16]. We seek to improve the resolution of such multi-level phase masks by additive processing of transparent resist, and using electron beam lithography together with thickness-controlled layers for phase-locking of the diffracted beams.

In this research, two-layered phase gratings have been formed in transparent dielectric resist (350 nm thick ma-N resist) in multiple processing steps by electron beam lithography. A thin SiO_2 layer was used to isolate the grating layers and followed with dual spin-coating steps to planarize the final resist coating layer. In this way, independent pattern control on each of the two layers was demonstrated on polymeric

dielectric materials. This method provided a three-level phase mask with 600 nm X- and Y-axis periodicity, first order beam efficiency of up to 3.5% for 800 nm wavelength light, and appropriate π/2 phase shift such that diamond-like 3D nanostructure could be fabricated in SU-8 photoresist. Because the polymeric resist was highly insulating and challenging to image by SEM, each nanostructure layer was verified by a soft-coating of conductive polymer that could be removed without substrate damage and thereby enable step-by-step SEM inspection. The 600 nm periodicity was selected to meet the important design challenge of reducing the axial-to-lateral period ratio (c/a) of the exposed 3D periodic structure to reach the ideal value of $c/a \approx \sqrt{2}$ [17] that predicts the widest expected PBG (i.e. 24-27% for inverted silicon [4, 18]) near the telecommunication wavelength of 1.5 μm. Experimental demonstrations typically report c/a values above ~3.6 [2, 6, 11, 15, 16]. The precision of e-beam writing is promising here for creating more advanced diffractive optical components based on multi-layered dielectric nano-grating masks, with benefits of inter-layer phase shift control that is not possible with traditional binary (single layer) phase masks.

2. Phase Mask Fabrication

The conceptual approach in forming two-layered phase masks in e-beam resist is outlined in Fig. 1. A glass substrate (Fig. 1a) was first coated with a single layer of transparent e-beam resist to a thickness tuned for optimal half wavelength of $\lambda/[2(n-1)]$ or π phase optical delay to maximize the 1st order diffraction efficiency. E-beam exposure and development of the resist were then used to form the one-dimensional (1D) binary grating as shown in Fig. 1b. A thin conformal silica isolation layer (Fig. 1c) served to physically and chemically isolate the first layer grating from a second resist coating, which upon additional e-beam patterning and development led to the crossed dual-layered nano-grating structure as depicted in Fig. 1d-i. To improve on an uneven coating thickness anticipated in the top resist layer (Fig. 1d-i), two or more successive spin-coatings of the resist were introduced to planarize the top surface of the second resist layer prior to e-beam patterning. In this way, smooth crossed grating lines are expected as shown in Fig. 1d-ii on which the multi-level phase mask can be based.

In order to verify the thickness, period and uniformity of the grating nanostructures at each processing step (Fig. 1b, 1c and 1d), a "soft" conformal coating of a conductive polymer was necessary for SEM inspection, for example, over the first grating surface as shown in Fig. 1b-i. A reversible conductive coating is desired that returns the sample to the original state.

Both positive- and negative-tone e-beam resists were tested to serve as transparent grating layers. Negative e-beam resist (micro resist technology GmbH, ma-N 2405) was spin-coated on glass at 3000 rpm for 30 s and baked at 90 ^{0}C for 90 s on a hotplate to yield a 350 nm thick film. A thin conductive layer (20 nm thickness) of either aquaSAVE (Mitsubishi Rayon) or Cr was deposited to assist with charge dissipation during the resist patterning with an electron beam lithography system (Vistec, EBPG 5000+) at an optimized 250 μC/cm^2 dosage. After exposure, the aquaSAVE or Cr layer was removed with a water wash or with CR-7 solution (Cyantek), following the manufacturer's recommendations. The photoresist was immersed in developer of ma-D 525 (micro resist technology GmbH) for 135 s and dried with Nitrogen gas flow. Alternatively, a positive-tone resist of ZEP 520A (ZEON Chemicals) was spin-coated on glass at 6000 rpm for 60 s and baked at 180 ^{0}C for 2 minutes on a hotplate to form a 360 nm thickness. Similar procedures were followed for conductive coating and removal, and e-beam exposure was optimized at 280 μC/cm^2 dosage. The resist was immersed in developer ZED-N50 (ZEON Chemicals) for 60 s, fixed in MIBK:IPA (9:1 in volume, MicroChem) solution for 30 s and dried in a Nitrogen gas flow.

In the case of positive-tone resist, e-beam exposure of a second resist layer was found to unavoidably penetrate and alter the underlying first layer. In the case of the negative-tone resist (ma-N), this problem was solved with a physio-chemical isolation layer. A conformal SiO_2 layer of 40 nm thickness was sputtered (AJA International, ATC Orion 8 Sputter Deposition System) over the first grating layer by the standard manufacturer procedure to provide a robust nano-grating substrate (Fig. 1c) on which second grating layer patterns could be generated and removed until the desired grating patterns (Fig. 1d-ii) were obtained. The second layer grating was formed with a similar procedure as the first layer. Spin rates were varied to independently control the layer thicknesses.

For SEM imaging (Hitachi, S3400 and S5200), a 20-nm thick conformal coating of aquaSAVE (Mitsubishi Rayon) was formed by dispensing directly over the grating layer (as in Fig. 1b-i) at 1000 rpm for 40 s and then baking at 90 ^{0}C for 60 s. Following SEM imaging, the polymer was removed by water wash, enabling a procedure for non-destructive inspection of the gratings. To verify that the aquaSAVE coating was sufficiently conformal, a single-layer grating was first formed in ZEP 520A e-beam resist into the square array pattern of 600 nm square holes as shown in the atomic force microscopy (AFM) image in Fig. 2a. The AFM scan was repeated (Fig. 2b) following a 20 nm soft coating of aquaSAVE. The cross-hole profiles (bottom images) of the uncoated and coated samples revealed nearly identical profile shapes with respective 360 nm and 350 nm hole depths, attesting to a conformal coating of 20nm thickness and ±10 nm variation.

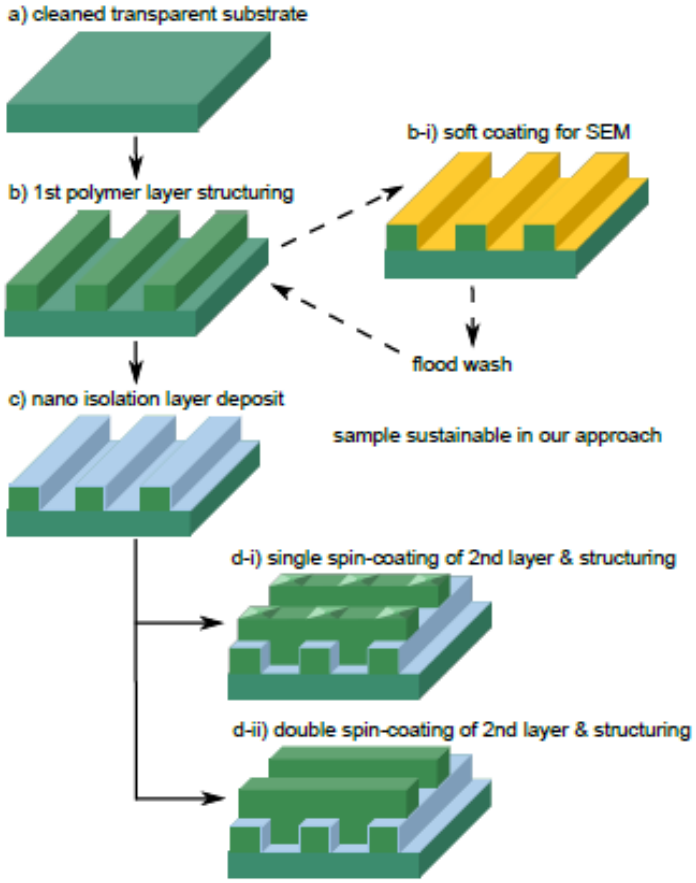

Fig. 1. Flow chart for processing a two-layered nano-grating mask. e-beam resist was spun over a glass substrate (a) and e-beam patterned to form a nano-grating (b), followed by silica conformal coating (c), on which second grating layer patterns by a single (d-i) or double spin-coating (d-ii) could be repeatedly generated and removed until the desired grating patterns were generated (d-ii). Such high-resolution e-beam written patterns were verified by SEM inspection (b-i). A conductive polymer was spin-coated to provide enhanced conductivity of the nanostructured sample for the SEM inspection, after which the sample was recovered by washing away the conductive polymer layer without damaging the lower nanostructures.

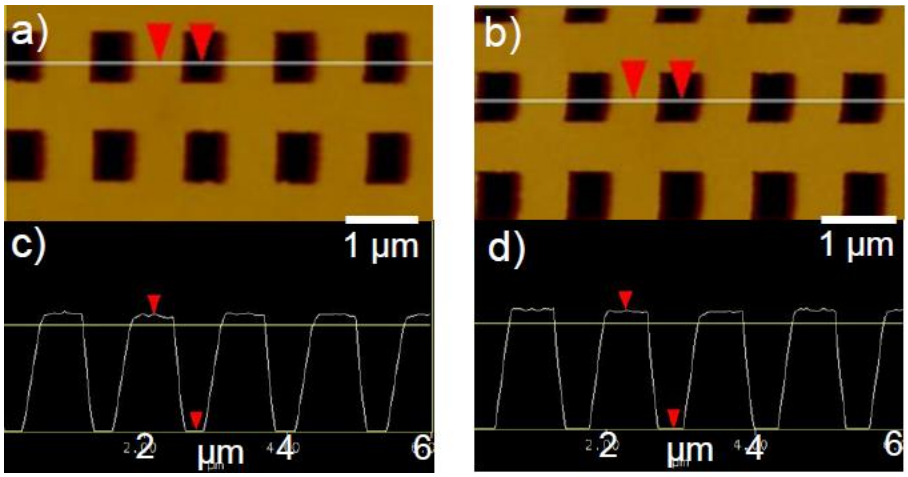

Fig. 2 Atomic force microscope (AFM) observation of conformal soft coating. Top view AFM images of a representative square hole (600 nm square) array sample patterned by e-beam lithography (a) before and (b) after aquaSAVE soft-coating. AFM profile images reveal similar profile-shape and ~360 nm thickness and ~350 nm of hole depth (c) before and (d) after aquaSAVE coating, respectively. The non-square shape in (d) is attributed to mismatch in stitching the horizontal scan lines as often occurs in AFM.

The higher resolution limits of the aquaSAVE coating was further examined over finer grating patterns formed in (2D) square arrays of 80-120 nm diameter round holes spaced with 400 nm X- and Y- periodicity on single-layer ZEP resist. Figure 3 shows low (a-d) and high (e-h) resolution SEM images of the uncoated resist grating (Fig. 3a and 3e), the soft-coated grating (Fig. 3b and 3f), and the grating after removal of the soft coating (Fig. 3c and 3g). One notes a significant reduction of the charging effects in Fig. 3a and 3e with the aquaSAVE coating (Fig. 3b and 3f) that enables highly resolved imaging of the holes. Close inspection (Fig. 3f) reveals a charging effect that is highly localized (~10 nm) and seen to amplify the imaging contrast at the edges of the hole perimeter. The reversibility of the coating process is noted by the return of the large-area charging effect in Fig. 3c and 3g, recorded after removal of the soft coating. The underlying grating could be further processed (Fig. 4 below) without any observable consequences arising from the aquaSAVE coating steps. A comparison of the soft coating (Fig. 3b and 3f) with a traditional Au coating (~20 nm) on the same grating structure (Fig. 3d and 3h) shows identical nano-structural features were resolved with similar precision, for example, the ~40 nm gap of the crack seen in this damaged film. Hence, the aquaSAVE offered a reversible conformal coating of good conductivity to enable high resolution SEM imaging of the dielectric nano-gratings at low 5 kV voltage.

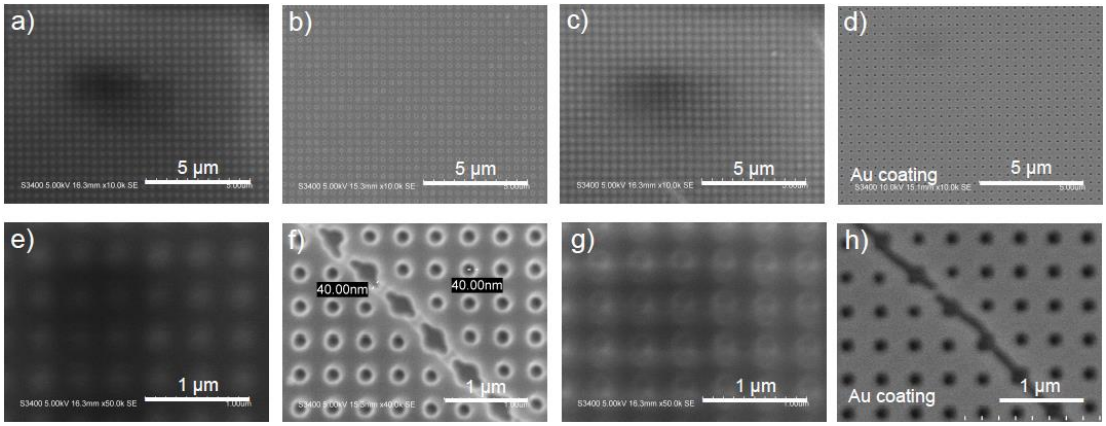

Fig. 3 SEM pictures of nanostructured e-beam resist (ZEP) at low (a-d) and high (e-h) resolution, recorded as formed (a, e), with a 20 nm aquaSAVE coating (b, f), after removal of the aquaSAVE coating (c, g), and with a Au coating (d, h). SEM voltage of 5 kV was used for all images except for the 10 kV value for (d).

Dual-layered grating structures (Fig. 4) were best formed with the negative-tone ma-N resist as noted above. A first layer of ma-N resist with a pattern of variable 2.5 and 1 μm width lines was e-beam fabricated and coated with aquaSAVE for the SEM imaging in Fig. 4a. After removal of the aquaSAVE, the grating was coated with the SiO_2 isolation layer and a single-layer coating of ma-N resist. Orthogonally oriented lines were patterned only into the top layer by e-beam, producing the SEM image in Fig. 4b after coating with aquaSAVE. Bumps were clearly visible at the overlapping lines in the SEM image (white arrow in Fig. 4b) and were verified by AFM to protrude by 50±5 nm for the narrowest crossing lines (1 μm width) as seen in Fig. 4c. To form a more uniform grating thickness, the 2nd resist layer was fully removed by acetone immersion to recover the original silica-coated first-layer resist as verified by the SEM image of Fig. 4d. Two sequential spin coatings of ma-N resist were deposited and processed by the same e-beam pattern, generating the more uniform double layer as noted by the SEM image in Fig. 4e. The crossed line gratings are seen by AFM in Fig. 4f to have produced three distinct layers, all with uniform layer thicknessess of 0, 350 nm and 680 nm to within ±5 nm variation. The formation of such gratings was verified to small grating periods of 400 nm while the thickness of individual grating layers could be varied in the spin coating steps to enable high-resolution and tunable phase level design of 2D 3-level phase masks.

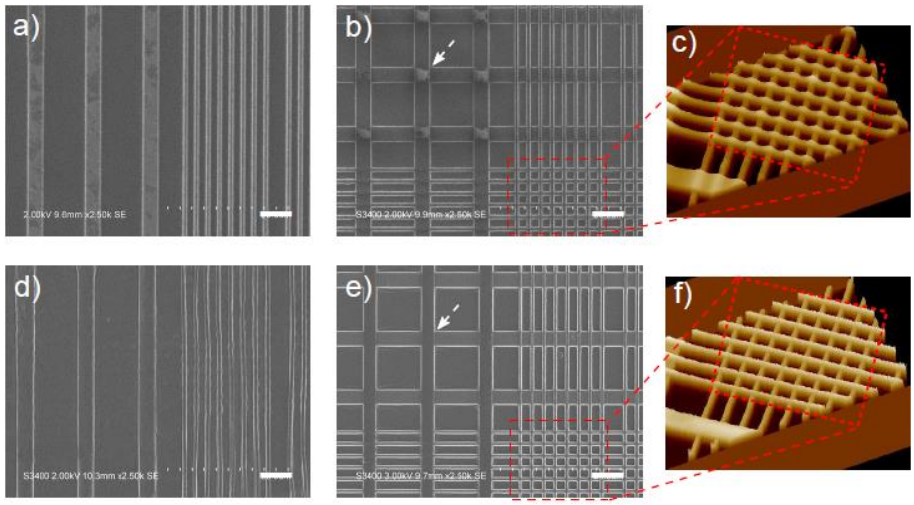

Fig. 4 SEM images of nanostructured e-beam resist (ma-N) showing (a,d) parallel 1D lines after coating with a 40 nm SiO_2 isolation layer and conductive polymer (aquaSave; 20 nm) and (b) crossed doubled-layered lines with single spin (b,c) and doubled (e,f) spin coatings of resist to form the second layer. Acetone washing of the sample in (b) recovered (d) the original first nanostructure layer, to permit re-processing with a double spin-coating to present a (d) more uniform top surface cross-line structure (compare white arrows in (b) and (e)). AFM profiles of samples (b) and (e) revealed surface variation of (c) ~50 nm and (f) < 10 nm, respectively. The scale bar is 5 μm.

3. A multi-level nano-grating phase mask: Design and optical performance

A 3-level phase mask design (Fig. 4f) was sought for holographic formation of 3D photonic crystal templates in photoresist with the potential for generating a 3D complete PBG in the telecommunication window around 1.5 μm wavelength. For inversion in high refractive index material such as silicon, an optimal c/a ratio in the range of 1.0 to 1.7 has been found in calculation [19] to provide wide band gaps for the case of diamond-like symmetry. PBG modeling with the plane wave expansion method [20] typically centers the stopband in this diamond-like case at $a/\lambda_{PBG} \approx 0.4$. This imposes a phase mask design with transverse period of $a \approx 600$ nm. When targeting a central c/a ratio of ~1.5 together with this small grating period, one requires a large illumination wavelength of ~886 nm that generates large diffraction angles of 67.4° in a typical photoresist (SU-8, n=1.6). For practical purposes, our design is shifted to a more practically available wavelength of 800 nm from a Ti:Sapphire laser.

A major challenge in the phase mask design was in overcoming the inherently low first-order diffraction efficiency available from this combination of sub-wavelength grating period (a/λ=600 nm/800 nm) and modest refractive index contrast (Δn=n-1=0.6) for ma-N resist and air phase mask. Theoretical calculation of 3D isointensity patterns were systematically applied for various grating patterns based on finite-difference time domain (FDTD) calculations of diffraction efficiency of the 0^{th} order (0°) and four primary 1^{st} order beams (67.4°) tilted azimuthally in symmetric ±X and ±Y directions. The interference intensity contrast generated by the phase mask was first examined as a function of the 0^{th} order intensity for the case of symmetric diffraction with equal efficiency amongst the four 1^{st} orders, and plotted in Fig. 5 for the cases of 0 (red) and π/2 (blue) phase shifts between the X- and Y-axis orthogonal orders. The interference contrast follows similar trends for both phase shift cases, with large contrast of ≥0.83 found once the 0^{th} order intensity falls below 80%. Bicontinuous 3D periodic structures are anticipated by the 3D isointensity patterns as shown in the center-left and center-right inset images for the respective BCT and diamond-like cases that arise from 0 and π/2 phase shifts, respectively. Lower 0^{th} order intensity will lower the axial contrast (vertically), eventually leading to the 2D-periodic structure shown as the left-most inset image for the extreme case of 0% intensity of the 0^{th} order beam. In the other direction, higher 0^{th} order intensity (>80%) reduces the interference contrast for all 3D directions, eventually leading to formation of a uniform solid structure as shown by the right-most image for both phase shift cases. At intermediate values of phase shift, for example, the values of π/8, π/4 and 3π/8 phase shift plotted (purple circle) at 80% of 0^{th} order intensity, the interference contrast was found to lie between the BCT (red) and diamond-like (blue) data curves.

Practical limits in the present phase mask design lead to very low 1^{st} order diffraction efficiencies that only reach a maximum of 7% and 5% for the 0 and π/2 phase shift cases, respectively, according to FDTD modeling. This restricts the practical range for phase mask exposure to 0^{th} order intensities above 72% (solid blue dot) and 80% (solid red dot), respectively in Fig. 5. However, sufficient 3D interference contrasts of greater than 0.5 are still available for 1^{st} order diffraction efficiencies of 0.75% and 1.5% for 0 and π/2 phase shift cases, respectively. The remaining challenge is to optimize the thickness and line-widths of the gratings in the dual phase mask layers for both large and symmetric efficiencies on the X- and Y-axes.

As a starting point of phase mask design shown conceptually in Fig. 6a inset, the full thickness (H_y) of the two phase mask layers of ma-N resist were set to $\lambda/[2(n-1)]$=667 nm to provide a π phase optical delay between the top and bottom grating surfaces that typically maximizes the 1^{st} order diffraction efficiency for our 800 nm source. After several iterations of balancing the orthogonal diffraction efficiencies, the X and Y oriented grating line thicknesses of H_x and H_y, respectively, were fixed at 350 nm and 700 nm, respectively, and followed by FDTD calculation of 1^{st} order diffraction efficiencies. Figure 6a plots the X-(blue) and Y-(red) diffraction efficiency generated by the thicker (H_x) and thinner (H_y) gratings, respectively, as a function of identical W_x=W_y grating line widths. One notes a high X-Y axis asymmetry in these 1^{st} order efficiencies with a peak efficiency of 6.4% on the Y axis (red) for grating line width of W_x=W_y=200 nm. However, a weaker symmetric efficacy of 2.85% is noted at the blue-red crossing point for grating line widths of W_x=W_y=295 nm. The diffraction efficiencies of the positive and negative 1^{st} orders are identical owing to the grating symmetry.

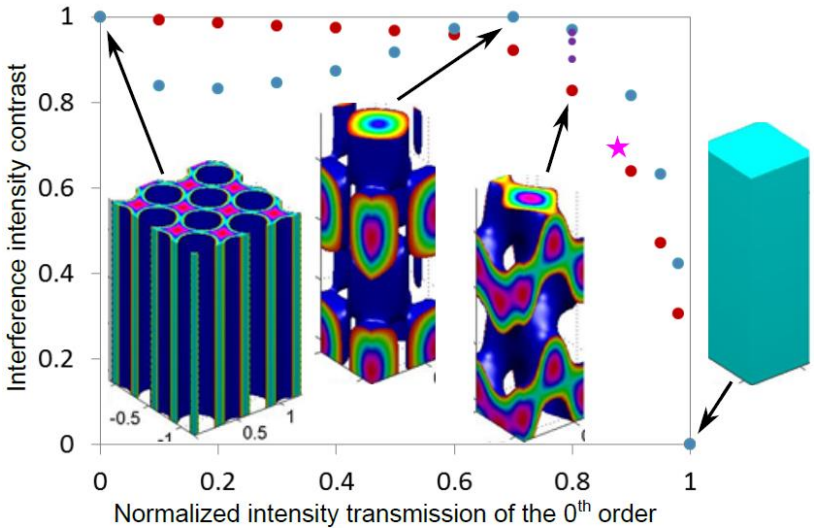

Fig. 5 Intensity contrast of the 3D interference pattern (0^{th}, and four equal intensity ±X and ±Y 1st order beams) generated holographically, plotted as a function of normalized 0^{th} order intensity for 0 (blue) and $\pi/2$ (red) phase shift in the orthogonal 1st order diffraction beams. The purple points (from top to down) result from orthogonal phase shifts of $\pi/8$ to $\pi/4$ and $3\pi/8$. The pink star is simulated for the 3-level phase mask of Fig. 7d. The four inset images are representative isointensity surfaces for the case of (left) 2D structure formed with zero intensity of 0th order beam, (middle left) 3D BCT structure formed with in-phase orthogonal diffracted beams, (middle right) 3D diamond-like structure formed with $\pi/2$ phase shift of orthogonal diffracted beams, and (right) uniform intensity in the limit of 100% intensity of the 0th order diffracted beam.

To examine for a higher symmetric diffraction efficiency, the grating width W_x was optimized (red square) for each value of W_y to generate the peak symmetric diffraction efficiency plotted (black diamond) in Fig. 6b as a function of the grating bar width W_y. The hatched zone eliminates impractical phase mask designs where high aspect ratio grating lines of $H_x/W_x \geq 1.75$ cannot be reproducibly generated in the present resist. Hence, an optimal phase mask design is identified for grating line widths of W_y=250 nm and W_x=280 nm to provide a balanced diffraction efficiency of 3.6%, in contrast with the lower 2.85% value found for the case of symmetric grating line widths of $W_x=W_y$=295 nm in Fig. 6a.

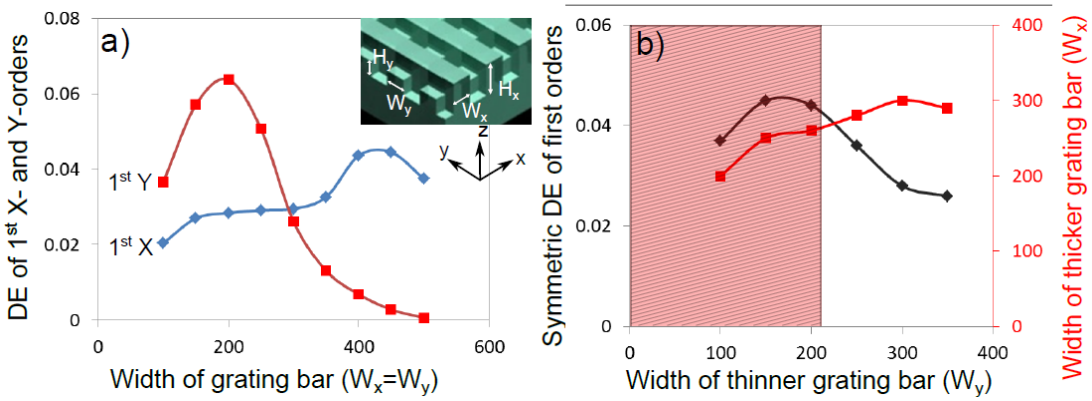

Fig. 6 (a) Diffraction efficiency of X- and Y-diffracted 1^{st} order beams of 800 nm wavelength, calculated by FDTD through a doubled-layer cross-grating phase mask (image inset) of 600 nm period, and plotted as a function of symmetric grating line widths such that $W_x=W_y$. (b) Similar diffraction calculation on the orthogonal X- and Y- 1^{st} order beams, plotted as a function of W_y grating width and showing the optimal grating line width of W_x for each W_y value that produces symmetric X- and Y- diffraction efficiency. The hatched zone requires unusually high aspect ratio ($H_x/W_x \geq 1.75$) grating lines. The phase mask layers (ma-N, n=1.6) were H_x=700 nm and H_y=350 nm thick.

Various single and two-layered phase masks were fabricated with the e-beam patterning procedures of section 2. The design schematic of binary and 3-level masks in Fig. 7a and 7b, respectively, resulted in the nanostructured e-beam resist shown by the SEM images in Fig. 7c and 7d, respectively. The 2D square array of holes in Fig. 7c was formed in a single-layer of 360 nm thick ZEP resist, while the two crossed linear gratings in Fig. 7d were formed with ≤50% duty cycle in two separate ma-N resist layers. An AFM image of this surface in Fig. 7e reveals phase mask layers with thicknesses of H_y=350 nm and H_x=700 nm.

Single-layer masks such as the one shown in Fig. 7c were evaluated for their diffraction efficiency with either an 800 nm femtosecond laser source (Spectra-Physics, Spitfire Pro 40F) or a 795 nm cw laser diode (Vixar Inc., custom package). Symmetric efficiencies meeting up to the theoretical maximum predicted at 5.4% were observed for the 1st orders in X- and Y-axes when W_x=W_y=250 nm. Dual layered phase masks such as in Fig. 7d were fabricated with a range of W_x and W_y values from 250 nm to 400 nm, producing symmetric and asymmetric 1st order diffraction efficiencies in the range of 2.7% to 3.6%. The highest symmetric efficiencies of 3.50% and 3.48% were measured for the Y- and X-axis 1st orders, respectively, for samples with W_y and W_x ranging within 270±20 nm and 290±10 nm, respectively. These values correspond well with the nearly optimal symmetric diffraction efficiency of 3.6% found theoretically for phase mask line widths of W_y=250 nm and W_x=290 nm as plotted in Fig. 6b for 600 nm period and 800 nm wavelength.

To evaluate the potential of the present 3-level phase mask for patterning photonic crystal templates, isointensity patterns were calculated for the binary and 3-level phase masks for the case of 800 nm wavelength exposure and symmetric 1st order diffraction efficiencies of 4.0 and 3.50%. The results shown in Fig. 7f and 7g for the respective binary and 3-level phase masks, show similar structural periodicities of 600 nm laterally and 1.13 um axially. After accounting for axial shrinkage typically observed at ~35% in SU-8 photoresist [21-23], one anticipates generating a c/a ratio of ~1.22 with the phase mask. The 3D symmetry of the isointensity patterns follow the expectation of BCT-like (Fig. 7f) for the binary mask and diamond-like tetragonal (Fig. 7g) for the multi-level mask. A higher magnified view of such 3D symmetry is shown in the inset pictures of Fig. 7f and 7g for the case of inversion of the photoresist template with a high index material such as silicon (n=3.45). Filling fractions of 0.55 and 0.34, respectively, were selected for optimal balancing of the 3D bicontinuity and generating the widest PBG.

A plane expansion method [20] was applied to the ideal inverted silicon nanostructure shown in Fig. 7f (inset) and 7g (inset) to produce the photonic band dispersion diagrams in Fig 7h and 7i, respectively. The BCT-like structure produced with the binary mask does not support a complete photonic band gap (Fig. 7h), generating only small directional stopbands such as in the Γ-Z direction. In contrast, the diamond-like structure produced with the multi-level mask presents a complete photonic band gap as indicated by the gray-colored zone in Fig. 7i. The photonic band gap is omni-directional, 8.2% wide and centered at a/λ=0.3866, which corresponds to a central stop band position at 1580 nm, close to the 1500 nm wavelength we initially targeted for the telecommunication band.

In order to verify the holographic fabrication of such 3D PBG templates, the presently optimized phase mask devices were exposed by a 800-nm femtosecond laser into thick photoresist (40 μm of unmodified SU-8, MicroChem) to drive two-photon absorption. However, a low laser coherence length of 3.5 μm precluded periodic structuring through the full 40-μm thickness of the resist and the phase masks were therefore tested with a non-optimal wavelength of 514.5 nm, provided by an Argon ion cw laser (Coherent, Innova Sabre MotoFred). For the dual layer phase mask, the top resist layer was reduced from 350 to 220 nm thickness (H_y-H_x) in order to provide the π/2 phase shift required on the X- and Y-oriented diffraction beams with this 514.5 nm source. To thin the layer, diluted ma-N resist was spun at a higher speed (6000 rpm/s) and a longer period of time (60 s) and repeated to planarize the top surface. Following previously optimized procedures, the photoresist was modified with 0.3% weight HNu-470 (Spectra Group Ltd.) photo-initiator and 2.5% OPPI co-initiator (Spectra Group Ltd.) [16, 23], exposed at ~400 mW/cm^2 uniform intensity for 5-20 s, soft-baked and post-baked over a temperature ramp of 65 ^{0}C and 95 ^{0}C in a period of 1 to 10 min, and immersed in SU-8 developer (MicroChem) for 6 to 10 min at room temperature. 3D photonic nanostructures were observed to be generated fully through the photoresist thickness, for example, as shown in the SEM top view images of Fig. 7j and 7k for the respective binary and double-

layered phase mask cases. The 3D nanostructures in Fig. 7j and 7k show the expected BCT and diamond-like woodpile symmetry, respectively, evidenced by respective square symmetry (Fig. 7j) and vertically offset X- and Y- oriented bars (Fig. 7k) that were generated by the 0 and $\pi/2$ phase shift differences in the respective phase mask layers. The inset of Fig. 7k shows a well-matched isointensity surface calculated for the present exposure conditions of symmetric 3.5% efficiencies of the individual first order beams generated by the incident 514 nm light.

Figure 7l (blue line) shows the normalized Γ-Z transmission that was measured through the sample of Fig. 7k to have formed a moderately strong stopband near 1.58 μm wavelength with 60 nm width (FWHM). The spectrum matches with the FDTD calculation (Fig. 7l, red line) that was inferred from the 3D nanostructure shown in Fig. 7k, predicting a stronger Γ-Z directional stopband with slightly wider width of 80 nm (FWHM). The present crystal structure will not support a complete PBG after inversion with silicon owing to the shorter exposure wavelength of 514.5 nm that imposed a higher 3D anisotropy ($c/a \approx 3.4$) in the 3D periodic structure. Nevertheless, the results demonstrated the valuable principles of the multi-level phase mask design and fabrication that may optimize 3D holographic exposure and produce wide stopband photonic crystal media.

3. Discussion and conclusion

In this work, the concept of dual-layer electron beam lithography (Fig. 1) was introduced to develop a multilevel phase mask from e-beam resist (Fig. 7d) that could offer high resolution grating features with phase offset control between orthogonal diffraction beams. The design of the mask was aimed at producing 3D nanostructure templates with potentially a wide complete photonic band gap in the telecommunication band. To this end, the resist layer thicknesses and grating widths were optimized (Fig. 5 and 6) for high and symmetric diffraction efficiencies on orthogonal diffraction orders and predicated to form high contrast 3D nanostructures with only modest 1^{st} order diffraction efficiencies of ~4% (Fig. 6b) as calculated by FDTD. This low efficiency was found sufficient to template 3D photonics crystal structures according to isointensity modeling (Fig.7f and 7g). The e-beam generated masks were exposed by Argon ion radiation to capture 3D photonic bicontinuous nanostructures in photoresist (Fig. 7j and 7k) and yield a measured Γ-Z directional stopband of 5.2% width (Fig. 7l). A plane wave expansion calculation for an 800 nm source revealed that a subsequent inversion of the 3D photonic structure with $\pi/2$ vertical phase shift into silicon material would open a complete photonic band gap with 8.2% size (Fig. 7i). Collectively, the numerical and experimental results have presented a new approach for flexible design and fabrication of high resolution multi-level grating masks with phase shift control.

Transferring such layered resist patterns into glass by etching [14] would improve the robustness of the phase mask surface. The selection of optical substrates with higher refractive index, for example, chalcogenide glass (n=2.45~3.2) [24] or SiN_x ($n \approx 2$) [25] films, would significantly improve the diffraction efficiency of the gratings, presently limited to individual 1^{st} order diffraction efficiency of ~6% (Fig. 6a) in the e-beam resist. Such high-index sub-wavelength phase masks would generate stronger interference contrast (i.e. <80% 0^{th} order diffraction in Fig. 5) and broaden the laser exposure window for opening bi-continuous 3D nanostructure during holographic lithography. Alternatively, the formation of additional grating layers on Talbot spaced planes may also be considered here to enhance the diffraction efficiency when constrained by low-index contrast gratings in this sub-wavelength limit [26].

The formation of 3D PC templates with diamond-like symmetry (Fig. 7k) clearly demonstrates the flexible utility of the e-beam written phase masks for encoding the diamond-like symmetry directly into the grating layer design. One bypasses the limitations of binary phase masks [4, 15] when applied in a single exposure step [Fig. 7j] or the limited phase shift control in multi-step or multi-mask holographic exposures [3, 5, 27] in controlling the symmetry of the interference light pattern. Further, e-beam lithography offers more consistent and higher resolution patterning than available by 3D laser direct-writing of similar diffractive optical elements [11, 14, 15, 28].

In conclusion, three-level nano-grating phase masks have been fabricated in electron-beam resist (ma-N) to meet with the requirement for holographic generation of diamond-like 3D nanostructure in SU-8

photoresist in a single exposure step. A multi-level 2D phase mask has provided a 600 nm period, first order diffraction efficiency of up to 3.5% for 800 nm wavelength illumination light that matched with the phase mask design value. A reversible soft-coating method (aquaSAVE) enabled SEM inspection and verification of each insulating grating layer. A thin SiO_2 layer was used to isolate the grating layers and multiple spin-coating steps served to planarize the final resist layer. Holographic lithography in SU-8 photoresist provided 3D periodic structure with diamond-like symmetry, verifying the $\pi/2$ phase shift generated in the orthogonal diffracted beams from the two grating layers. A simulation of 800 nm exposure of the phase mask was found to provide an anticipated 8.2% complete PBG when inverted in silicon. The e-beam patterning method is extensible to assembling multiple layers of nanophotonic structure for generating new types of diffractive optical elements.

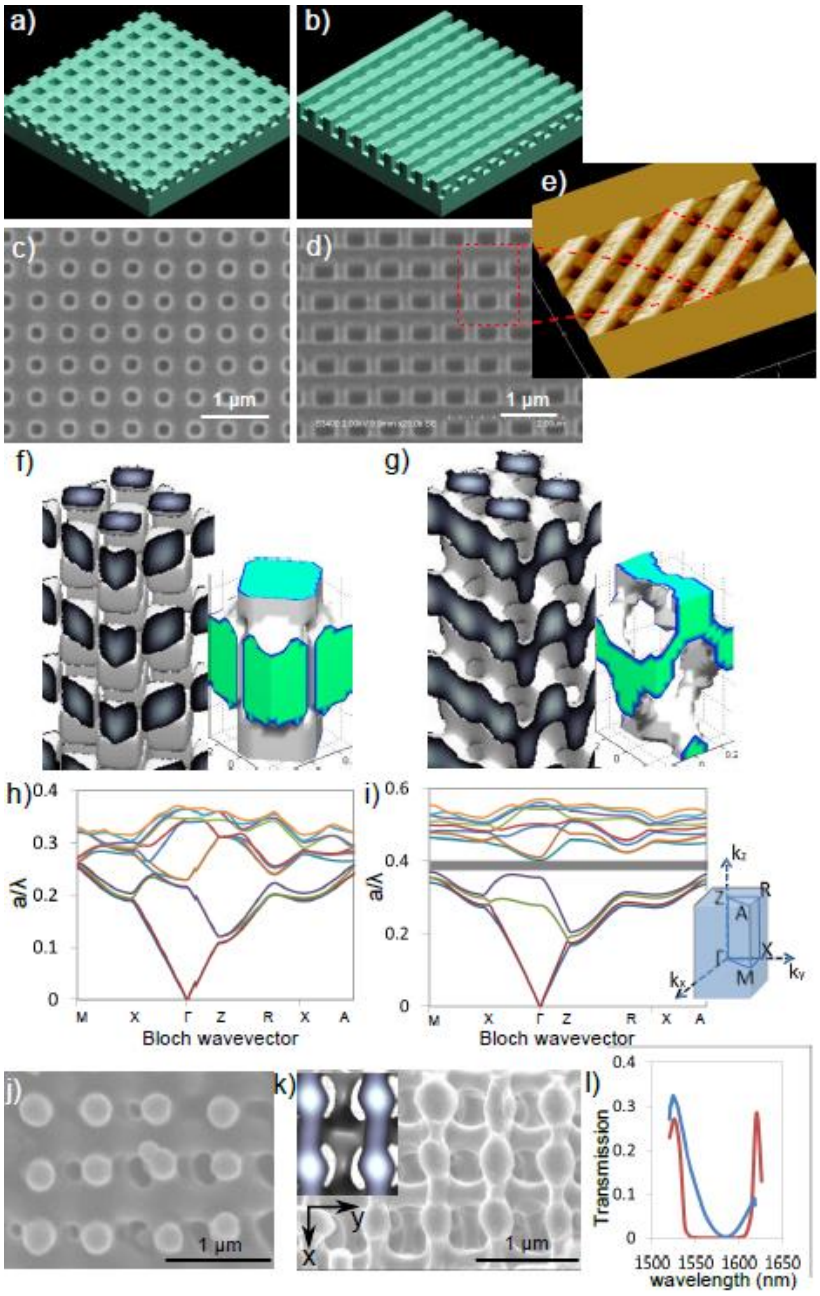

Fig. 7 Comparison of (a) a binary and (b) a three-level phase mask design and SEM images (c) and (d), respectively, of the associated structures formed by e-beam lithography in ma-N resist. When these 600 nm period masks are illuminated with 800 nm wavelength light to expose photoresist, respective (f) BCT-like and (g) diamond-like 3D symmetry structures are expected to form according to isointensity calculations. If inverted with a high index material such as Si (inset images), bandgap, photonic bandgap dispersion calculations reveal formation of an (h) incomplete photonic and (i) a complete photonic band gap (8.2% width), respectively. The positions of the high-symmetry points in the reciprocal lattice for both (h) and (i) were shown in the inset of (i). SEM images (j) and (k) of SU-8 photoresist exposed by 514.5 nm light through the masks in (c) and (d), respectively, revealing the expect BCT and diamond-like structural symmetry. The structure in (k) is seen to be well matched with the simulated isointensity (inset). (h) The measured (blue) and the FDTD-simulated (red) normal incidence spectra for transmission through the photonic crystal template in (k).

References

[1] V. Berger, O. Gauthier-Lafaye and E. Costard, Photonic band gaps and holography. *J. Appl. Phys.*, 1997, **82**, 60.

[2] S. Jeon et al., Fabricating complex three-dimensional nanostructures with high-resolution conformable phase masks. *PNAS* 2004, **101**, 12428-12433.

[3] Y. Lin, P. R. Herman and K. Darmawikarta, Design and holographic fabrication of tetragonal and cubic photonic crystals with phase mask: toward the mass-production of three-dimensional photonic crystals. *Appl. Phys. Lett.*, 2005, **86**, 071117.

[4] T. Y. M. Chan, O. Toader and S. John, Photonic band-gap formation by optical-phase-mask lithography. *Phys. Rev. E*, 2006, **73**, 046610.

[5] I. Bita, T. Choi, M. E. Walsh, H. I. Smith and E. L. Thomas, Large-area 3D nanostructures with octagonal quasicrystalline symmetry via phase-mask lithography. *Adv. Mater.* 2007, **19**, 1403-1407.

[6] Y. K. Lin, A. Harb, D. Rodriguez, K. Lozano, D. Xu and K. P. Chen, Fabrication of two-layer integrated phase mask for single-beam and single-exposure fabrication of three-dimensional photonic crystal, *Opt. Express*, 2008, **16**, 9165-9172.

[7] T. Y. Jeon et al., 3D hierarchical architectures prepared by single exposure through a highly durable colloidal phase mask. *Adv. Mater.* **26**, 1422-1426 (2014).

[8] J. E. Elek, X. A. Zhang, B. Dai, Z. Xu and C.-H. Chang, Fabrication of three-dimensional hierarchical nanostructures using template-directed colloidal assembly. *Nanoscale*, 2015, **7**, 4406-4410.

[9] S. Noda, K. Tomoda, N. Yamamoto and A. Chutinan. Full three-dimensional photonic bandgap crystals at near-inrared wavelengths. *Science*, 2000, **289**, 604-606.

[10] J. Valentine, S. Zhang, T. Zentgraf, E. Ulin-Avila, D. A. Genov, G. Bartal and X. Zhang, Three-dimensional optical metamaterial with a negative refractive index. *Nature*, 2008, **455**, 376-379.

[11] Q. Xu, Y. Lv, C. Dong, T. S. Sreeprased, A. Tian, H. Zhang, Y. Tang, Z. Yu and N. Li, Three-dimensional micro/nanoscale architectures: fabrication and applications. Nanoscale, 2015, 7, 10883-10895.

[12] C. F. Guo et al., Grayscale photomask fabricated by laser direct writing in metallic nano-films, Opt. Express 2009, **17**, 19981-19987.

[13] J. D. Rogers et al., Realization of refractive microoptics through grayscale lithographic patterning of photosensitive hybrid glass. Opt. Express **12**, 1294-2004 (2004).

[14] M. Karlsson, K. Hjort and F. Nikolajeff, Transfer of continuous-relief diffractive structures into diamond by use of inductively coupled plasma dry etching. *Opt. Lett.*, 2001, **26**, 1752-1764.

[15] D. Chanda, L. E. Abolghasemi, M. Haque, M. L. Ng and P. R. Herman, Multi-level diffractive optics for single laser exposure fabrication of telecom-band diamond-like 3-dimensional photonic crystals. *Opt. Express*, 2008, **16**, 15402-15414.

[16] L. Yuan, M. L. Ng and P. R. Herman, Femtosecond laser writing of phase-tuned volume gratings for symmetry control in 3D photonic crystal holographic lithography. *Opt. Mater. Express*, 2015, **5**, 515-529.

[17] K. M. Ho, C. T. Chan, C. M. Soukoulis, R. Biswas and M. Sigalas, Photonic band gaps in three diemonsions: New layer-by-layer periodic structures. *Solid State Commun.*, 1994, **89**, 413-416.

[18] G. Y. Dong et al., Holographic design and band gap evolution of photonic crystals formed with five-beam symmetric umbrella configuration. *Opt. Express*, 2006, **14**, 8096-8102.

[19] D. Chanda, L. Abolghasemi and P. R. Herman, One-dimensional diffractive optical element based fabrication and spectral characterization of three-dimensional photonic crystal templates. *Opt. Express*, 2006, **14**, 8568-8577.

[20] K. M. Ho, C. T. Chan and C. M. Soukoulis, Existence of a photonic gap in periodic dielectric structures, *Phys. Rev. Lett.* 1990, **65**, 3152-3155.

[21] Y. K. Pang, J. C. W. Lee, C. T. Ho and W. Y. Tam, Realization of woodpile structure using optical interference holography. *Opt. Express*, 2006, **14**, 9113-9119.

[22] D. C. Meisel et al., Shrinkage precompensation of holographic three-dimensional photonic-crystal templates. *Adv. Mater.*, 2006, **18**, 2964-2968.

[23] L. Yuan and P. R. Herman, Laser Scanning Direct-Write Holography for Flexible 3D Fabrication of Multi-Scale Integrated Nano-structures, submitted.

[24] S. Wong, M. Deubel, F. Perez-Willard, S. John, G. A. Ozin, M. Wegener and G. von Freymann, Direct Laser Writing of Three- Dimensional Photonic Crystals with a Complete Photonic Bandgap in Chalcogenide Glasses. *Adv. Mater.*, 2006, **18**, 265-269.

[25] A. B. Djurisic and E. H. Li, Modeling the index of refraction of insulating solids with a modified lorentz oscillator model. *Appl. Opt.*, 1998, **37**, 5291-5297.

[26] M. L. Ng, D. Chanda and P. R. Herman, Coherent stitching of light in multiplayered diffractive optical elements. *Opt. Express*, 2012, **20**, 23960-23970.

[27] G. Liang, X. Zhu, Y. Xu, J. Li and S. Yang, Holographic Design and Fabrication of Diamond Symmetry Photonic Crystals Via Dual-Beam Quadruple Exposure. *Adv. Mater.*, 2010, **22**, 4524-4529.

[28] M. Mikutis, T. Kudtius, G. Slekys, D. Paipulas and S. Juodkazis, High 90% efficiency Bragg gratings formed in fused silica by femtosecond Gauss-Bessel laser beams. *Opt. Mater. Express*, 2013, **3**, 1862-1871.